Pattern phase diagram of spiking neurons on spatial networks

Dionysios Georgiadis
Future Resilient Systems, Singapore and Department of Management, Technology and Economics, ETH Zurich, Switzerland

Didier Sornette
Department of Management, Technology and Economics, ETH Zurich, Switzerland

(Received 19 December 2018; revised manuscript received 9 March 2019; published 19 April 2019)

We study an abstracted model of neuronal activity via numerical simulation and report spatiotemporal pattern formation and criticallike dynamics. A population of pulse coupled, discretized, relaxation oscillators is simulated over networks with varying edge density and spatial embeddedness. For intermediate edge density and sufficiently strong spatial embeddedness, we observe a spatiotemporal pattern in the field of oscillator phases, visually resembling the surface of a frothing liquid. Increasing the edge density results in a distribution of neuronal avalanche sizes which follows a power law with exponent one (Zipf's law). Further increasing edge density yields metastability between pattern formation and synchronization, before transitioning entirely into synchrony.

DOI: 10.1103/PhysRevE.99.042410

I. INTRODUCTION

Pulse coupled oscillator models (PCOs) are defined as populations of relaxation oscillators, interacting in a pulselike manner over some topology. Such models have provided insight into the phenomenon of spontaneous synchronization across fields, be it swarms of blinking fireflies, pulsing heart cells [1], distributed computing systems [2,3], or traders in financial markets [4,5]. PCOs have been prominent in neurology, since they can demonstrably capture multiple features of the rich dynamic behavior of biological neuronal systems, such as metastability (with the same configuration alternating between synchronous and asynchronous behavior) [6], spatiotemporal pattern formation (in the form of nonlinear waves) [7–11], and critical dynamics [6,12,13].

Models used in this literature range from intricate (such as the Hodgkin-Huxley model) to relatively simple (such as integrate and fire oscillators). Deville and Peskin [6] studied a population of discretized integrate and fire (DIF) oscillators, arguably the most abstracted neuronal model to date. In spite of its simplicity, the DIF model with all-to-all stochastic interactions can successfully capture metastability and synchrony [6], as observed in cortical networks. However, the extent to which the DIF can replicate the phenomenology of its more intricate counterparts is not well understood, which is the motivation for the present paper.

Numerical studies have considered the DIF over quenched nontrivial topologies, focusing either on synchrony in complex networks [14] or on replicating temporal features of biological neuronal networks [13]. Notably, in Ref. [13], populations of cascading spiking neurons in laboratory-grown cortical slices were found to follow a power law distribution as well as a specific temporal profile. Both these features were captured by a single simulation of a DIF model over a regular lattice, revealing that criticallike behavior is possible in DIF models. In Ref. [15] the DIF model was analytically shown to be critical for random graphs, and conditions for criticality were derived. However, criticality in spatial DIF models remains little understood, in spite of the recent interest around criticality in neuronal systems [16–18]. Furthermore, pattern formation in DIF models has not been studied at all.

To address these two issues, we consider the DIF over topologies ranging between two purposefully picked extremes: a random graph (which has been studied the most in the literature so far) and a spatial graph (which does not disregard the spatial nature of biological systems). Our results showcase that spatial embeddedness endows the DIF model with pattern formation and criticallike dynamics, and therefore the unrealistic all-to-all annealing topology drastically restricts the phenomenology of the DIF. Specifically, for sufficiently low spatial embeddedness, the field of oscillator phases forms a spatiotemporal pattern, visually reminiscent of the surface of a frothing liquid. Increasing the connection density results in metastability between pattern formation and synchrony (a behavior of biological neuronal networks [7]), while the transition itself is characterized by criticallike dynamics. For even higher connection density, near-periodic synchronous firing of all neurons ensues.

II. THE MODEL

Consider N identical oscillators over a undirected unweighted graph $\mathcal{G}$. Each node is associated with a binary *state* a_i (1 fired, 0 not fired) and a discrete, non-negative *phase* ϕ_i. We initialize all oscillator phases uniformly at random, and all states at zero. We then apply a *stochastic drive*, by randomly picking a small population of d oscillators and increasing their phase by one unit.

a. Dynamics: Once the phase of an oscillator reaches the *threshold* value Θ the oscillator is said to *fire*: its state is set to one, and the phases of all its neighbors are increased by one. This pulselike interaction results in avalanching events, which

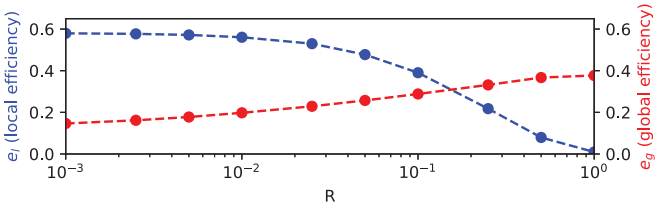

FIG. 1. Effect of long-range connectivity R on the topological properties of a spatial graph with 1000 nodes and mean degree 10 (see Sec. II, paragraph b). For increasing R, local efficiency e_l drops and global efficiency e_g rises [e_l, e_g defined in (1)], indicating a gradual change from local to global strong connectivity.

we will refer to as *cascades*. The cascade continues as long as new oscillators fire under the influence of their neighbors. Crucially, an oscillator is *only allowed to fire once* per cascade, a property dubbed refractoriness. This is realized in the model through the state a_i: an oscillator may fire only if its state starts from zero. Thus, once the oscillator fires, and its state is set to one, it is unable to fire again. The state remains one until the cascade ceases. Then all fired oscillators are reset: $(a_i, \phi_i) \leftarrow (0, 0)$, $\forall\{i : a_i = 1\}$. After resetting all fired oscillators, we resume the stochastic drive, until a new cascade starts. The number of oscillators that participated in the cascade is *the cascade size*.

b. Topology: The graph $\mathcal{G}$ is a random geometric graph [19], furnished with long-range connections. Random geometric graphs are arguably the most parsimonious models of spatial networks, constituting a canonical choice for the current study. For N nodes, average degree E, and a ratio of long-to-short range connections R, graph $\mathcal{G}$ is assembled as follows:

(1) "Sprinkle" N points uniformly at random over a one-by-one square space, with periodic boundaries.

(2) Find the *unconnected* pair of points with the minimum Euclidean distance and connect them. Repeat, until $E(1-R)$ edges have been drawn. We will refer to these edges as *short-range connections*.

(3) Pick ER random pairs of nodes and connect them, forming the *long-range connections*.

For low R we obtain a meshed, highly clustered graph. As R increases, the graph gradually loses its spatial character: long-range connections reduce clustering and increase navigability (a transition known as the *small-world* effect [20]). Navigability and clustering can be quantified by the *global efficiency* ($e_g \in [0, 1]$) and *local efficiency* metrics ($e_l \in [0, 1]$), respectively [21]. For unweighted graphs, e_g, e_l are defined as

$$e_g = \frac{e(\mathcal{G})E}{N-1} \quad \text{and} \quad e_l = \sum_{i\in\mathcal{G}} \frac{e(\mathcal{G}_i)}{N}, \tag{1a}$$

$$\text{where} \quad e(\mathcal{G}) = \frac{1}{N(N-1)} \sum_{i\neq j\in\mathcal{G}} \frac{1}{d_{ij}}, \tag{1b}$$

and where $\mathcal{G}_i$ is the subgraph of node i and its neighbors, and d_{ij} is the minimum number of hops needed to travel from i to j. The effect of R on the two metrics is shown for an example network in Fig. 1.

c. Additional nomenclature: We measure time in discrete "long" time, where an additional cascade corresponds to an additional "long" time unit. In contrast, "short" time is associated with the dynamics within a cascade. A total of n_s cascades are simulated, and the fractional size of the tth cascade is denoted by c_t ($c_t = 0$ implying no cascading). The phases ϕ_i form a field $\Phi_t = (\phi_0, \ldots, \phi_N)$. Both c_t and Φ_t vary in time, forming time series: $C = (c_0, \ldots c_{n_s})$ and $\Phi = (\Phi_0, \ldots, \Phi_{n_s})$. Both C and Φ are dependent on the parameters E, R, Θ, N. However, for the sake of notational simplicity, these dependences will remain implicit unless necessary.

d. Simulation parameters: Throughout the study, we fix $\Theta = 5$, $d = N/10^3$. We simulate 5×10^4 cascades, discarding the first 10^4 events, to ensure that the dynamics have reached stationarity. This results in $n_s = 4 \times 10^4$. Parameters R, E, and N are specified for each experiment.

III. IDENTIFYING REGIMES

For sufficiently high mean degree E, we observe *near-periodic synchrony*: cascades of scale $O(N)$ over regular time intervals. We quantify this behavior with the help of the metric $h \in [0, 1]$, which is formally defined as the normalized Herfindahl index of the temporal power spectrum of C, the time series of cascades on the "long" time process. Values of h near 1 correspond to asynchrony, and h near 0 implies synchrony. For the sake of succinctness details on this method can be found in Appendix A.

For sufficiently low R (less than approximately 0.21) and for a range of E, we observe a spatiotemporal pattern in the Φ field: low-phase *patches* are separated by high-phase *"fences"* (see bottom row of Fig. 2). The pattern constantly shifts: cascades are more likely to occur along the "fences," relaxing the oscillators and leaving a low-phase patch where a fence once stood. Simultaneously, cascades are unable to propagate through large patches and instead stop in their midst, leaving a "fence" where a patch was. We dub this spatiotemporal behavior *froth*.

The impact of connection density on the frothing behavior is depicted in rows 1 and 4 of Fig. 3. The size of the patches increases along with E, until the patches grow to percolate from top to bottom. Since each patch is the imprint of a past cascade, patch sizes are linked to cascade sizes. Consequently, this behavior can also be observed in the respective complementary cumulative probability distribution (CCDF) of cascade sizes, presented in rows 2 and 4 of Fig. 3.

As E increases, patches are enlarged, and the cascade size CCDF extends farther towards the right. Eventually, the CCDF forms a truncated power law with exponent one, producing what is often referred to as Zipf's law [22]. At the same point, the probability of a global sized patch becomes nonzero, indicating that spatial correlation length increases beyond the system size. The presence of the truncated power law and the increasing spatial correlation length is empirical evidence of the system being near a self-organized critical state. Simulating systems of increasing size reveals that the truncation point moves towards the right as N increasing, indicating that the near-critical behavior is not a finite-size effect (see Appendix B for details). Further increasing E, results in a cascade size distribution typical of supercritical

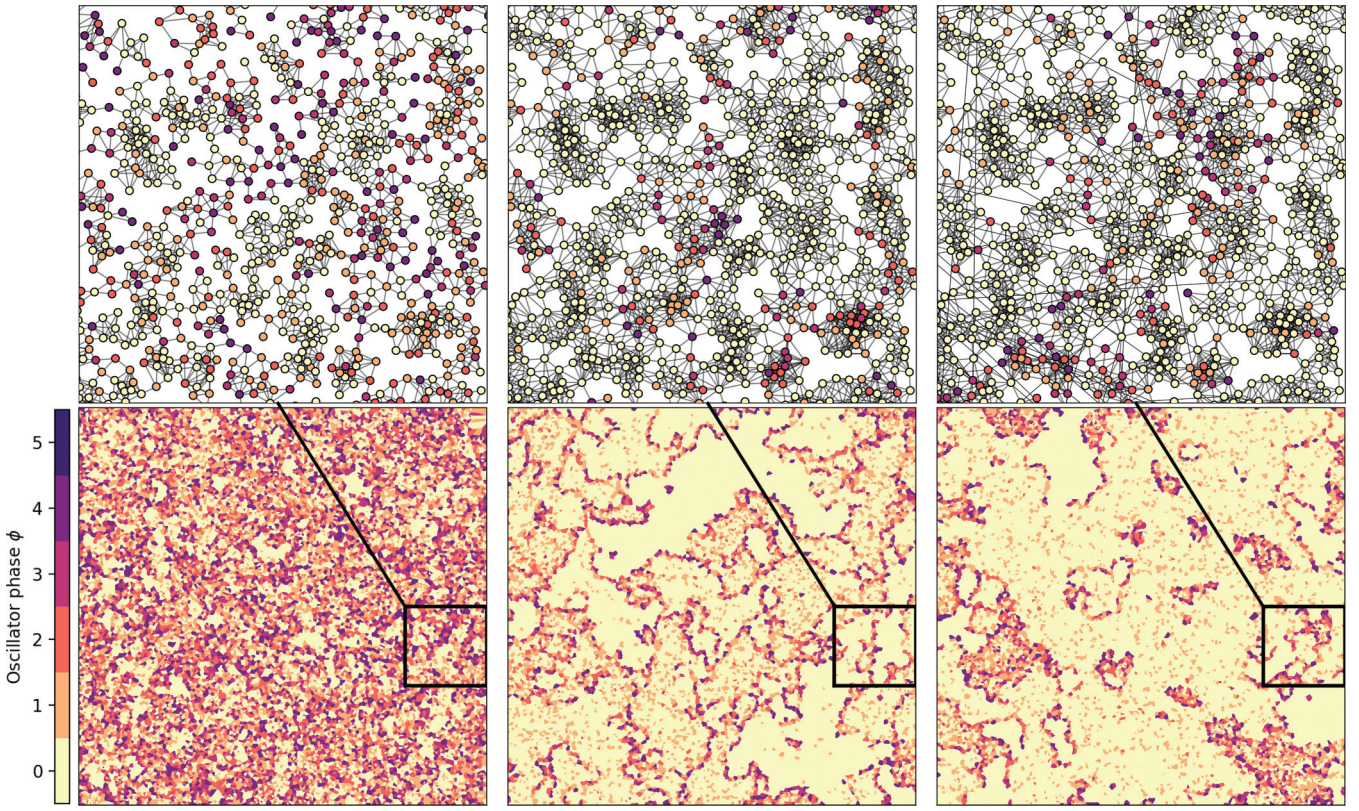

FIG. 2. Pattern formation and connectivity in a graph with $20k$ nodes. Columns correspond to graphs with different edge density E and long-range connectivity R [left to right (E, R) is $(7, 0)$, $(12, 0)$, $(12, 0.02)$]. *Bottom row:* visualization of oscillator phases ϕ; note the formation of synchronized patches. *Top row:* magnified segment of the graphs producing the dynamics below (as delineated by the black frame). Note the increased synchrony in densely meshed node clusters. Increased E enlarges the patches, and increased R enables global synchrony.

dynamics. An example of supercritical frothing is depicted in the bottom right panel of Fig. 3. Note the global-sized patch (connected top-to-bottom) indicating spatial correlation length comparable to the system size.

To quantify the presence of froth, and the associated scale of the patches, we consider

$$s_\Phi(\vec{\lambda}) = \left\langle H_t^2(\vec{\lambda}) \right\rangle, \tag{2}$$

where $H_t(\vec{\lambda})$ is the spatial Fourier transform of Φ_t for the wavelengths $\vec{\lambda} = [\lambda_1, \lambda_2]$, and $\langle . \rangle$ is the average of multiple realizations over time. We exploit the radial symmetry of the model by taking the radial mean of $s_\Phi(\vec{\lambda})$:

$$\mathcal{S}_\Phi(\lambda) = \frac{1}{2\pi|\lambda|} \int_{\Omega_\lambda} s_\Phi(\vec{\lambda})\, d\Omega_\lambda, \tag{3}$$

where Ω_λ is a circular shell of radius $\lambda = ||\vec{\lambda}||$.

Rows 3 and 6 of Fig. 3 reveal that frothing is accompanied by a power law increase of $\mathcal{S}_\Phi(\lambda)$. The increase starts from a low limit of λ, associated with the average spatial distance between oscillators neighboring in the two-dimensional Euclidean space, and persists up to a wavelength where $\mathcal{S}_\Phi(\lambda)$ forms a "knee." The wavelength associated with the "knee," dubbed the *corner wavelength* and denoted by χ, corresponds to the largest spatial scale up to which the froth exhibits a random, self-similar symmetry, as seen in rows 1 and 4 of Fig. 3.

These observations allow us to numerically quantify the presence of froth and the size of the patches, by fitting a truncated power law over $\mathcal{S}_\Phi(\lambda)$ (see the red line in rows 3 and 6 of Fig. 3). The fitting method places the power law truncation point at a wavelength that approximates χ. Also, the goodness of fit (given by $r^2 \in [0, 1]$) quantifies how well $\mathcal{S}_\Phi(\lambda)$ follows a truncated power law. Details about this method can be found in Appendix C.

The metric h [defined in Appendix A, Eq. (A2)] can be used along with r^2, to define *empirical criteria* for the identification of synchrony and frothing. Concretely, with m_h, m_{r^2} being two threshold constants, we have

$$h(E, R, N, \Theta) \begin{cases} > m_h, \text{ asynchrony} \\ \leqslant m_h, \text{ synchrony} \end{cases}, \tag{4a}$$

$$r^2(E, R, N, \Theta) \begin{cases} > m_{r^2}, \text{ frothing up to scale } \chi \\ \leqslant m_{r^2}, \text{ no frothing} \end{cases}. \tag{4b}$$

IV. TRANSITION DYNAMICS

The previously proposed criteria (4) require estimates for the thresholds m_{r^2}, m_h, which we obtain through the experiment presented in the current section. R and N are sampled geometrically (as defined in Fig. 4), while E takes 75 values evenly spaced in [5,20]. The results, shown in Fig. 4, reveal abrupt transitions in the macroscopic behavior, allowing us to draw three conclusions:

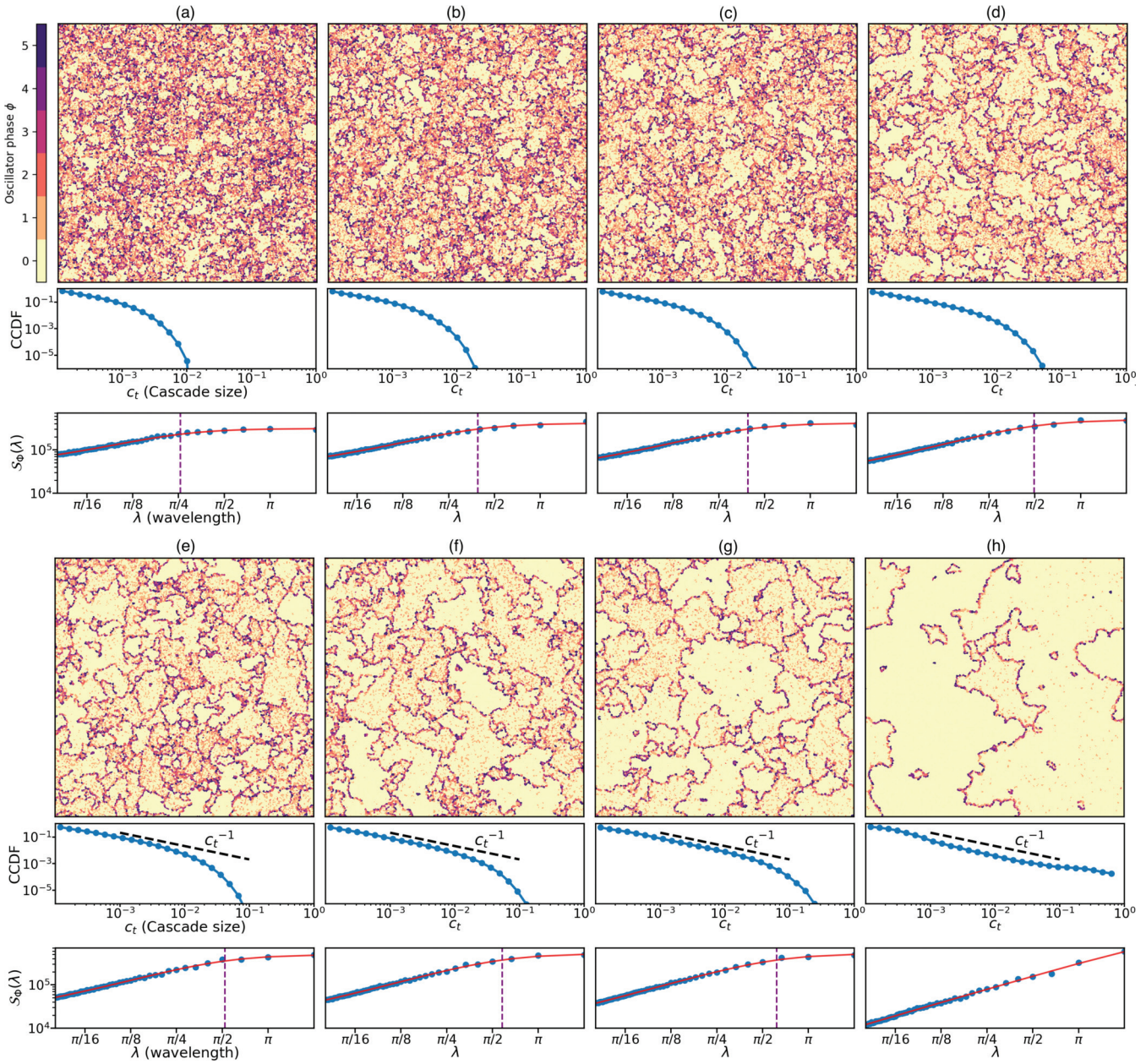

FIG. 3. *Rows 1 and 4:* snapshots of the oscillator phase fields Φ_i. Long-range connectivity R is zero. The mean degree E increases in the reading direction: left to right and top to bottom E is 10, 11, 12, 13, 14, 15, 16, 18. The scale of the patterns χ increases along with E. *Rows 2 and 5:* CCDF of cascade sizes for the simulations of the respective column. As χ increases, the CCDF extends towards the left, at first forming a power law and eventually a supercritical distribution (bottom rightmost panel). *Rows 3 and 6:* blue dots correspond to the temporal average of the spatial spectral power $\mathcal{S}_\Phi(\lambda)$ defined in (3). The solid red line is a truncated power law fit of $\mathcal{S}_\Phi(\lambda)$, and the purple (dashed) line is the corner wavelength χ, as determined by the method described in Appendix C.

e. Transition to synchrony: In the top row of Fig. 4 we observe a sharp transition, from high to low h, implying that the system suddenly moves from asynchrony to synchrony beyond a value of E. As R increases, the transition shifts to smaller E values, showing that spatial embeddedness delays the onset of synchrony. The sharpness of the transition increases with system size, revealing that this transition will still be present—and even more prominent—in the thermodynamic limit.

f. Frothing delays synchrony: The second row in Fig. 4 depicts a clear plateau of the r^2 metric, implying the presence of frothing dynamics over a range of E values. The frothing regime is interposed between asynchrony and synchrony, with its width decreasing as R increases. Therefore, while high R systems enter synchrony, low R systems froth instead, implying that frothing is the mechanism that delays synchrony. The presence of the frothing regime does not depend on size, since the plateau of r^2 persists—and even widens—along with N.

g. Scaling of χ: The bottom row of Fig. 4 shows that the corner frequency χ increases with N. Specifically, for the range of values in this study (N from $1.25k$ to $40k$) plotting $\chi\sqrt{N}$ makes simulation results for all N to collapse into a

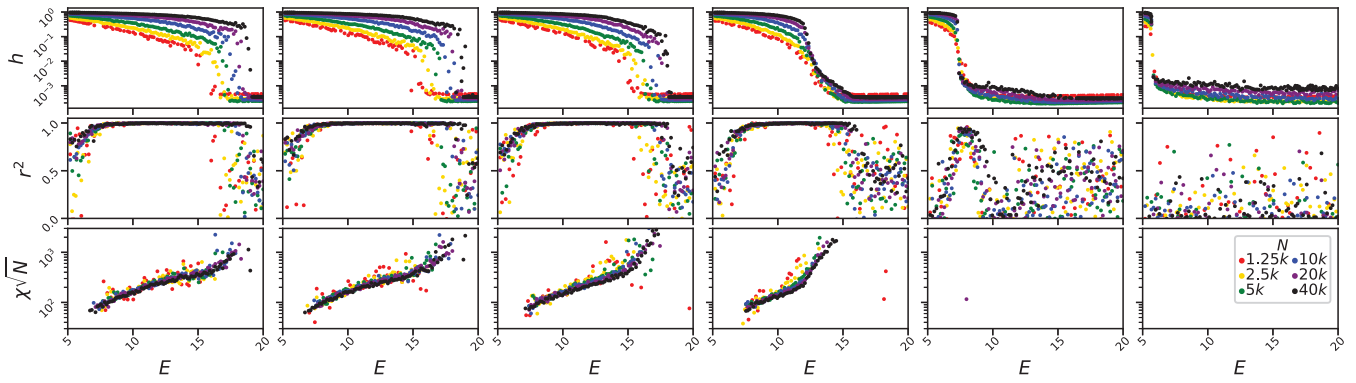

FIG. 4. Transitions in the DIF system: h, r^2 and $\chi\sqrt{N}$ (defined in Eq. (A2), Appendix C paragraph 4, and Sec. III paragraph 5) as functions of the mean degree E, for a number of system sizes N, with colder colors indicating larger system sizes ($1.25k, 2.5k, 5k, 10k, 20k, 40k$). Long-range connectivity R is 0.1%, 0.4%, 1.6%, 6.25%, 25%, 100% from left to right. Low values of h indicate synchrony, and r^2 near one implies the presence of spatiotemporal patterns. Missing points in the bottom row indicate the absence of pattern formation, for the two largest R values. Note the transitions (i) from high to low values of h and (ii) ascending and descending to a plateau of r^2. The sharpness of both transitions increases with N, demonstrating that larger systems exhibit more prominent patterns and sharper transitions between macroscopic behaviors.

single universal curve, revealing the presence of a scaling law. Finally, for all panels in the bottom row of Fig. 4, the peak of χ coincides with the end of the r^2 plateau, verifying that frothing patterns become the most prominent on the verge of synchrony.

V. EMPIRICAL REGIME DIAGRAM

To numerically investigate the macroscopic behavior of the model over the E, R space, we fix $N = 10^4$ and vary R over 70 evenly spaced values in the range [6, 20]. E takes 30 geometrically spaced values in $[10^{-3}, 1]$. In order to use the criteria (4), we need to set m_h, m_{r^2}. Visual inspection of the results in Fig. 4 reveals that $m_h = 5 \times 10^{-2}$ and $m_{r^2} = 0.9$ allow criteria (4) to separate the macroscopic regimes adequately well for illustrative purposes. The resulting empirical regime diagram is depicted in Fig. 5, revealing four regimes:

Regime I: For low connection density the system exhibits local cascades, with no frothing. The literature [6,23] refers to this regime as *asynchrony*.

Regime II: For low long-range connectivity, and over a midrange of E, frothing appears in the Φ field. We refer to this regime as a *frothing regime*.

Regime III: Starting from froth and sufficiently increasing E results in a regime where we intermittently observe the phenomenology of regimes II and IV. The CCDF of cascade sizes is characteristic of a supercritical system, with slower than power law decay, and global-sized cascades appearing regularly. This regime is dubbed a *metastable regime*.

Regime IV: For high connection density, the system undergoes a discontinuous limit cycle. As the average phase increases with time, cascades remain local in scale, until a global-sized cascade occurs, resulting in the relaxation of the phase field. Then the buildup of phase synchronization begins anew. We refer to this regime as *synchrony*.

VI. DISCUSSION

We have numerically investigated the behavior of discretized integrate and fire oscillators, with slow stochastic drive, over spatial graphs. Remarkably, when placed over spatial topologies these models give rise to nontrivial dynamics: spatiotemporal patterns form, where large clusters of relaxed nodes act as natural barriers against cascading, while jagged strips of near-firing nodes facilitate long distance propagation of cascades. This pattern can give rise to critical dynamics with cascading events sizes following a power law with exponent one. Further increasing the number of edges results in metastability between pattern formation and synchrony, and eventually drives the model into synchrony.

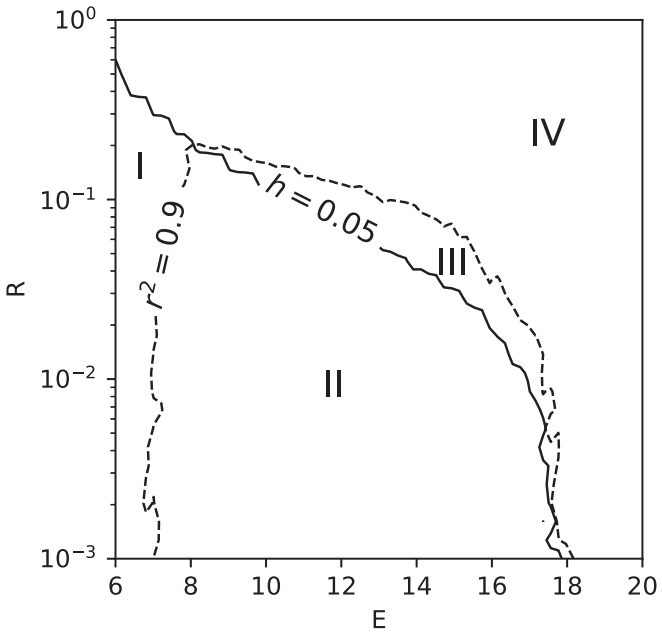

FIG. 5. Empirical regime diagram of the DIF model over the space of degree density and long-range connectivity (E, R). We observe four regimes: asynchrony (I), pattern formation (II), synchrony (IV), and metastability between pattern formation and synchrony (III). The regime boundaries are drawn based on the criteria defined in (4).

Our findings show that taking into consideration the fundamentally spatial character of neuronal networks drastically extends the phenomenological overlap between the DIF and more intricate neuronal models. Specifically, while previous works have already indicated that spatial embeddedness may delay the onset of synchrony [24], we showcase that the underlying mechanism is spatiotemporal pattern formation. This observation provides solid grounds for the usage of the DIF model in the study of pattern formation and critical dynamics in neural networks. Further numerical studies could shed light on the role of additional neuronal properties (leakiness, nonlinear response curves, and inhibition) on pattern formation and criticality in neuronal systems.

The presented model can also account for the evolution of the macroscopic behavior of laboratory-grown neuronal systems. As laboratory-grown neuronal networks mature, dendrites grow longer connecting neurons more densely over longer distances [25,26]. In our analysis, this process can be understood as an increase of long-range connectivity and overall connection density (parameters R and E). We therefore expect to see different dynamical regimes as the system matures: from subcritical dynamics to near-periodic synchrony. Indeed, this has been observed in practice: as laboratory-grown cultures mature, they exhibit near-periodic global cascades [25–27]. More crucially, in such cultures, cascades that do not grow to reach global proportions follow a truncated power law [26], a property also captured by the studied model (see Sec. V, regime III).

In spite of the extensive simulations in the current study, the exact mathematical nature of the regime transitions of the model is not well understood—and could constitute the subject of future works. Additionally, to the best of the authors' knowledge, frothing has not been so far empirically observed in physical systems. This is surprising considering the generality of the conditions under which frothing arises. A possible explanation could be that detecting froth requires knowledge of the *phase*, an attribute of oscillators that is typically less prominent and harder to measure than their *state*. In any case, further works are warranted, focusing on the empirical detection of frothing in pulse coupled oscillator systems.

ACKNOWLEDGMENTS

D.G. would like to thank S. C. Lera and S. O. P. Blume for stimulating discussions and is supported by the Future Resilient Systems at the Singapore-ETH Centre (SEC), a collaboration between ETH Zurich and National Research Foundation (NRF) of Singapore (FI 370074011), under the auspices of the NRF's Campus for Research Excellence and Technological Enterprise (CREATE) program.

APPENDIX A: QUANTIFYING SYNCHRONY

The near-periodic behavior of the time series of cascade sizes C can be detected in the frequency domain, where peaks appear in the power spectrum. The concentration of the spectral power around these peaks is quantified using the Herfindahl-Hirschman index. Since the data are discrete, we will be using the discrete Fourier transform. Let $\mathcal{P}_C(f)$ be the temporal *spectral power* of C for frequency f:

$$\hat{h} = \sum_f \left[\frac{\mathcal{P}_C(f)}{\mathcal{N}}\right]^2, \quad \mathcal{N} = \sum_f \mathcal{P}_C(f), \tag{A1}$$

$$h = \frac{\hat{h} - n_s}{1 - n_s}. \tag{A2}$$

The $\hat{h}$ metric takes values in [0,1] and quantifies the concentration of $\mathcal{P}_C(f)$ around a few frequencies. During asynchrony, the only significantly contributing frequency is the zeroth, resulting in near-zero values of $\mathcal{P}_C(f)$ for $f > 0$ and therefore h near one. In contrast, during synchrony, higher harmonics carry considerable amount of power resulting in a lower h index. Discerning between synchrony and asynchrony does require a threshold value of h, which we determine empirically in this study to be equal to 5×10^{-2} (see Section V paragraph 1 for details).

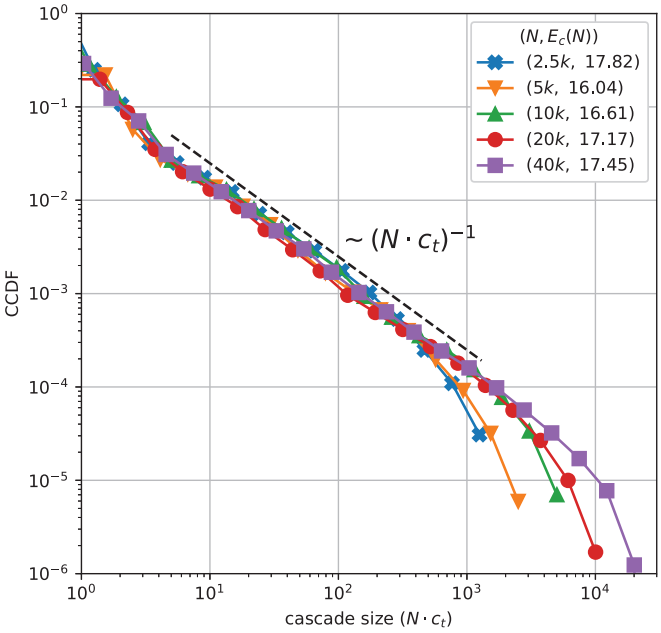

FIG. 6. CCDF of cascade sizes, for increasing system size N and zero long-range connectivity $R = 0$. The CCDF forms a truncated power law of exponent one (as indicated by the black dashed line). The truncation point moves farther to the right as N increases, indicating that the truncation is a finite-size effect. The overall network density E differs for each system size N.

APPENDIX B: CASCADE SIZE CCDF FOR INCREASING SYSTEM SIZE

In order to ensure that the observed criticallike dynamics are not due to a finite-size effect, we simulate increasing system sizes for $R = 0$ and for 70 values of E linearly spaced in the range [6,20]. For each system size, a value of E can be found for which the truncation point of the power law moves at its rightmost. We dub this value $E_c(N)$. The CCDF of cascade sizes for connection density $E_c(N)$ is shown in Fig. 6. The simulated system sizes, along with the corresponding $E_c(N)$, can be found in the legend of the same figure. The plotted CCDFs reveal that the power law truncation point is moving farther towards the right as N increases, indicating

that the truncation is a finite-size effect, and therefore that the simulated systems are indeed near criticality.

APPENDIX C: QUANTIFYING SPATIOTEMPORAL PATTERN FORMATION

We observe that in the case of frothing patterns, $\mathcal{S}_\Phi(\lambda)$ follows a power law increase, over a band of wavelengths. The upper limit of the band χ is associated with the largest cell size of the frothing pattern. The lower limit of the band is proportional to the size of the mesh used to estimate the Φ field. In the current study, $\sqrt{N}$ oscillators are placed along each dimension of the two-dimensional Euclidean space, resulting in an lower wavelength limit of $4\pi/\sqrt{N}$.

Higher frequency components also reside in the Φ field, for example due to the randomness in the placement of the oscillators. These higher frequency components may introduce noise in the spatial spectrum of Φ, through a process known as *aliasing*. Specifically in the case of data produced by processes with power law spectra, aliasing results in the measured spectrum progressively resembling white noise as we move to smaller wavelengths [28]. As a treatment, we ignore the values of the measured spectrum for small wavelengths, by doubling the lower limit derived in the previous paragraph to $\lambda_{\min} = 8\pi/\sqrt{N}$.

To determine the corner wavelength χ, we consider the frequency response function of a linear low-pass filter:

$$g(\lambda; p_1, p_2, p_3, p_4) = \frac{p_1}{\sqrt{1 + (\lambda/p_3)^{-2p_4}}} + p_2 \qquad \text{(C1)}$$

and fit it to $\mathcal{S}_\Phi(\lambda)$, according to the following equation:

$$(p_1^*, p_2^*, p_3^*, p_4^*) = \underset{\substack{p_1,p_2,\\ p_3,p_4}}{\operatorname{argmin}} \sum_{\lambda \geqslant \lambda_{\min}} \left[\frac{\mathcal{S}_\Phi(\lambda) - g(\lambda; p_1, p_2, p_3, p_4)}{\mathcal{S}_\Phi(\lambda)} \right]^2, \qquad \text{(C2)}$$

where p_1, p_2, p_3, p_4 are fitting parameters. Equation (C1) describes a power law increase with exponent p_4, up to the wavelength p_3 where the function forms a visual "knee." From that point onwards, the value of (C1) remains nearly constant at $p_1 + p_2$. For the sake of illustration, and to enable comparison between different $\mathcal{S}_\Phi(\lambda)$ curves, we position the truncation point χ at p_3^*.

Initial solutions to the problem in (C2) were obtained via the particle swarm method, and refined with a Levenberg-Marquardt local search. Examples of the fitted $g(\lambda; p_1^*, p_2^*, p_3^*, p_4^*)$ are depicted in rows 3 and 6 of Fig. 3 (red solid line), along with the corresponding $\mathcal{S}_\Phi(\lambda)$ values. The quality of the fits can be assessed via the r-squared metric, to which we will refer to as r^2. Specifically, r^2 is used to determine whether a simulation exhibits frothing: a high value of r^2 implies that Eq. (C1) provides a good fit, providing evidence in support of the presence of froth in the Φ field.

[1] R. E. Mirollo and S. H. Strogatz, SIAM J. Appl. Math. **50**, 1645 (1990).
[2] A. V. Proskurnikov and M. Cao, IEEE Trans. Automat. Contr. **62**, 5873 (2017).
[3] K. Konishi and H. Kokame, Chaos **18**, 033132 (2008).
[4] C. M. Wray and S. R. Bishop, Sci. Rep. **4**, 6355 (2014).
[5] C. M. Wray and S. R. Bishop, PloS ONE **11**, e0151790 (2016).
[6] R. E. L. DeVille and C. S. Peskin, Bull. Math. Biol. **70**, 1608 (2008).
[7] X. Huang, W. C. Troy, Q. Yang, H. Ma, C. R. Laing, S. J. Schiff, and J.-Y. Wu, J. Neurosci. **24**, 9897 (2004).
[8] H. R. Wilson and J. D. Cowan, Biophys. J. **12**, 1 (1972).
[9] R. E. L. DeVille, E. Vanden-Eijnden, and C. B. Muratov, Phys. Rev. E **72**, 031105 (2005).
[10] G. B. Ermentrout and D. Kleinfeld, Neuron **29**, 33 (2001).
[11] X. Guardiola and A. Díaz-Guilera, Phys. Rev. E **60**, 3626 (1999).
[12] S. Bottani, Phys. Rev. Lett. **74**, 4189 (1995).
[13] N. Friedman, S. Ito, B. A. W. Brinkman, M. Shimono, R. E. L. DeVille, K. A. Dahmen, J. M. Beggs, and T. C. Butler, Phys. Rev. Lett. **108**, 208102 (2012).
[14] R. E. L. DeVille and C. S. Peskin, Bull. Math. Biol. **74**, 769 (2012).
[15] J. P. Gleeson and R. Durrett, Nat. Commun. **8**, 1227 (2017).
[16] J. M. Beggs and D. Plenz, J. Neurosci. **23**, 11167 (2003).
[17] O. Kinouchi and M. Copelli, Nat. Phys. **2**, 348 (2006).
[18] J. M. Beggs, Philos. Trans. R, Soc, Lond. A **366**, 329 (2008).
[19] M. Penrose *et al.*, *Random Geometric Graphs* (Oxford University Press, Oxford, 2003), Vol. 5.
[20] D. J. Watts and S. H. Strogatz, Nature (London) **393**, 440 (1998).
[21] V. Latora and M. Marchiori, Phys. Rev. Lett. **87**, 198701 (2001).
[22] A. Saichev, Y. Malevergne, and D. Sornette, *Theory of Zipf's Law and Beyond* (Springer, Berlin, Germany, 2010).
[23] R. L. DeVille, C. S. Peskin, and J. H. Spencer, Math. Modell. Nat. Phenom. **5**, 26 (2010).
[24] L. Hernández-Navarro, J. G. Orlandi, B. Cerruti, E. Vives, and J. Soriano, Phys. Rev. Lett. **118**, 208101 (2017).
[25] H. Yamamoto, S. Moriya, K. Ide, T. Hayakawa, H. Akima, S. Sato, S. Kubota, T. Tanii, M. Niwano, S. Teller *et al.*, Sci. Adv. **4**, eaau4914 (2018).
[26] J. G. Orlandi, J. Soriano, E. Alvarez-Lacalle, S. Teller, and J. Casademunt, Nat. Phys. **9**, 582 (2013).
[27] E. T. Martorell, A. A. Ludl, S. Rüdiger, J. G. Orlandi, and J. Soriano, IEEE Trans. Netw. Sci. Eng. (2018), doi:10.1109/TNSE.2018.2862919.
[28] J. W. Kirchner, Phys. Rev. E **71**, 066110 (2005).